State-space Model and Analysis of Motion-induced Eddy-current based on Distributed Current Source Method

Bingjie Hao, Xiaoshu Liu, Kok-Meng Lee*, *Fellow, IEEE/ASME* and Kun Bai, *Member, IEEE*

***Abstract*—This paper presents a distributed current source method to model the motion-induced eddy-current and its damping force. The proposed method, which relaxes two commonly made assumptions (negligible mutual induction and small vibration), discretizes the conductor into elemental vibrating current-density sources as state variables. The motion-induced eddy-current model has been formulated in state-space representation, and validated numerically with FEA; the results show excellent agreement. The model provides a basis to investigate the effects of mutual induction and vibration amplitude on the computation accuracy of the eddy-current and its generated magnetic flux density and damping force. The findings reveal existing methods (based on these commonly made assumptions) overestimating the peak damping force, and failing to capture high-order harmonic components and frequency effects on phase-shift. Results of a parametric study that investigates the effects of the PM aspect ratio and conductor skin-depth on the damping force are presented, providing essential bases for design optimization of EC damping system control applications.**

***Index Terms*—Eddy current, state-space, vibration control, damping force, damper**

I. Introduction

Eddy current (EC) can be induced in a moving conductor under a stationary or alternating magnetic field. The current will generate a Lorentz force on the conductor, which is a repulsive, or damping, force against the motion [1]. Based on the motion direction and types, the damping forces are widely used in various industrial applications. For example, the eddy current damping torque in a rotational motion can be used for braking in automobile [2]. In vertical vibrations, the damping force is utilized to develop various EC dampers that can be applied to structural vibration suppression to replace traditional tuned mass damper due to their contactless, cost-effective, and self-powered characteristics [3]. Laborenz *et al*. investigated the EC damper in mitigating the vibration of steam turbine blading for turbomachinery applications. to [4]. Ebrahimi *et al.* designed a magnetic spring-damper system that has the potential to be used in automobile suspension [5]. High damping coefficient can be achieved in the damper by optimizing the permanent magnet (PM) configuration [6]. Yang *et al*. developed a vibration suppression device for the milling of thin-walled workpiece where chatter vibration happens due to the low rigidity of workpiece [7][8]. Dampers using PMs as magnetic sources are called passive dampers. However, a magnetic field can also be generated by an electromagnetic coil to achieve active damping [9]. Unlike in the above applications, where EC and the damping force induced in a moving conductor are used as effective tools, in some applications, such as maglev positioning system [10] and high-speed magnetic flux leakage testing [11], the parasitic EC and damping force during motion are unwanted. Their characteristics must be analyzed to achieve better control or improved accuracy.

Models for solving the motion-induced EC, the consequent damping forces, and the EC-generated magnetic flux density (MFD) have been widely studied. Esposito proposed an integral formulation for the analysis of electromagnetic fields distributions in systems where bodies are in motion [12]. The method is based on the subdivision of conductive regions and can be used for modelling 3D EC problems. Peng *et al.* proposed a finite element-based composite grid method that uses separate mesh grids to model a moving conductor [13], while Muramatsu *et al.* analyzed the steady state EC using a moving coordinate system [14]. Pluk *et al.* modeled the EC damper on a finite rectangular conducting plate by using image method to account for the boundary effect [15]. These models can provide accurate solutions for EC problems, but require solving complicated mathematical equations, and the relations between the damping force and the motion are not intuitive, thus hard to be incorporated into the dynamic analysis of damping devices. Therefore, in the design and analysis of EC dampers, simplified models derived from analytical solutions are often used. Sodano *et al.* established an EC damping model for a cantilever beam with magnetic field generated by a PM in [16]. Similar models were used in [4] and [7] to design dampers for steam turbine blading and milling applications. In these models, a cylindrical PM and a conducting plate are often used to facilitate the calculation of magnetic field and the induced EC. Some assumptions are made to simplify the model. In modeling magnetic fields, [4, 7, 16] used a constant MFD for a given point on a vibrating beam, given that the vibration

Research supported in part by the U. S. National Science Foundation under Grant CMMI-1662700, and in part by the National Basic Research Program of China (973 Program) under Grant 2013CB035803. The work of B. Hao was supported by China Scholarship Council.

B. Hao is with the State Key Lab. of Dig. Manuf. and Equip. Tech. (SKL-DMET), Huazhong Univ. of Sci. and Tech. (HUST), Wuhan, 430074, China and currently a visiting scholar at Georgia Inst. of Tech.

K.-M. Lee* and X. Liu are with the George W. Woodruff Sch. of Mech. Eng. at Georgia Inst. of Tech., Atlanta, GA 30332-0405, USA. K.-M. Lee is also Distinguished Professor of SKL-DMET at HUST, Wuhan, 430074, China.

K. Bai is with the SKL-DMET at HUST, Wuhan, 430074, China

* *Corresponding author email*: kokmeng.lee@me.gatech.edu.

Manuscript 324 submitted to IEEE/ASME International Conference on Advanced Intelligent Mechatronics. Received March 7, 2019.

displacement is small. As for the calculation of EC, mutual induction (MI) was neglected due to its relatively small contribution compared to the magnetic field of the PM. By ignoring the MI effect, the original EC problem, which is a typical PDE problem, is converted into a problem of solving algebra equations. However, these assumptions cannot always be satisfied. The influences of the assumptions must be analyzed and discussed.

In this paper, a straightforward and accurate model for solving the EC in a vibrating conductor is proposed and formulated in a state-space representation, which makes it applicable to control applications such as active damping studies. The MI effect is accounted for by using the distributed current source (DCS) method [17], which has previously been applied and validated in modeling the EC induced through a time-varying magnetic field excitation. The remainder of the paper offers the followings:

- A DCS method for modeling the motion-induced (2D axisymmetric) EC in state-space representation is presented, providing a basis to investigate the effects of commonly used assumptions applied on the computation accuracy of the EC and its generated MFD and damping force.
- The DCS model that relaxes commonly made assumptions has been validated numerically by comparing results with FEA simulated using commercial software.
- The parametric effects of the PM aspect ratio and conductor skin-depth on the damping force for a forced vibration were studied numerically.

II. Model

Figure 1 shows the characteristic parameters and coordinate system of a typical EC system for deriving the damping force due to the motion-induced EC in a conductive plate (radius r_p and thickness h) that vibrates with displacement $z = Z_o \sin(\omega t)$ and velocity $w=dz/dt$. The static magnetic field is generated by a circular PM (radius a_o, length $2a$ and magnetization $\mathbf{M}=M_0\mathbf{e}_z$) that is placed normal to the conductive plate. The ECD $\mathbf{J}$ can be derived by (1) where σ is the electric conductivity, $\mathbf{v}$ is the plate velocity and $\mathbf{B_m}$ and $\mathbf{B_c}$ are the MFD contributed by the PM and EC respectively:

$$\mathbf{J}=\sigma\mathbf{v}\times\left(\mathbf{B_m}+\mathbf{B_c}\right) \tag{1}$$

As shown in (1), $\mathbf{B_c}$ that accounts for the mutual induction (MI) in the conductor has an influence on $\mathbf{J}$ and hence on the Lorentz force $\mathbf{F}$ acting on the conductor, which can be derived from (2) by integrating over the volume $\mathcal{V}$ of the conductor:

$$\mathbf{F}=\int_{\mathcal{V}}\mathbf{J}\times\mathbf{B_m}\,d\mathcal{V} \tag{2}$$

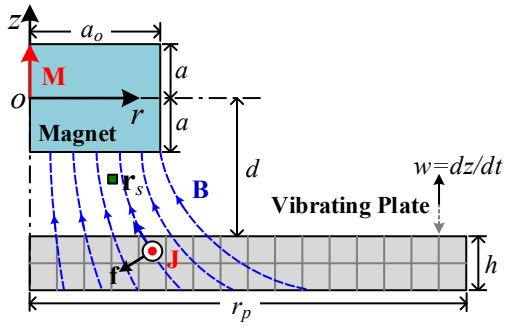

Fig. 1 Schematics of EC system in vibrating conductor

The ECD cannot be directly measured but can be characterized by measuring the EC-generated MFD in space. For a point at $\mathbf{r}_s$, $\mathbf{B_c}$ can be expressed as

$$\mathbf{B_c}\left(\mathbf{r}_s\right)=\int_V\frac{\mathbf{J}\times\left(\mathbf{r}_s-\mathbf{r}\right)}{\left|\mathbf{r}_s-\mathbf{r}\right|^3}dV \tag{3}$$

In most literatures that analyze the vibration-induced EC, the EC-generated MFD is often ignored (viz. $\mathbf{B_c}=0$) for simplicity when calculating ECD through (1), in which case the ECD, the damping force, and the measured EC-generated MFD are approximately proportional to the vibration velocity. To account for the MI effects on the ECD, the conductor is decomposed into n annular elemental current sources as illustrated in Fig. 1 using the DCS model as follows.

A. State-space Model for a 2D-axisymmetric system

To facilitate characterizing the mutual induction among the current sources, the magnetic vector potential (MVP) $\mathbf{A}$ (defined by $\mathbf{B}=\nabla\times\mathbf{A}$ and $\nabla\bullet\mathbf{A}=0$) is introduced. Expressed in cylindrical coordinates (assigned at the PM center as shown in Fig. 1), the i^{th} elemental ECD source at (r_i, z_i) is written as

$$\mathbf{J}_i=-\sigma\frac{\partial}{\partial t}\left(\mathbf{A_m}_i+\sum\nolimits_{j=1}^{n}\mathbf{A_c}_{ij}\right) \tag{4a}$$

where $\mathbf{A_c}_{ij}=f(r_{ij})V_i\mathbf{J}_j$; (4b)

$$f\left(r_{ij}\right)=\frac{\mu_0}{4\pi}\int_0^{2\pi}\frac{\cos\theta d\theta}{\sqrt{(r_i-r_j\cos\theta)^2+(r_j\sin\theta)^2+(z_i-z_j)^2}}. \tag{4c}$$

In (4a), $\mathbf{A_m}$ and $\mathbf{A}_{cij}$ denote the MVP generated by the PM and that by the j^{th} element on the i^{th} element, respectively. In (4b), V_i is the element volume; and $f(r_{ij})$ is a kernel function.

For a 2D-axisymmetric system, $\mathbf{J}_i=[0\ J_i\ 0]^{\text{T}}$ has only a circumferential component; and hence $\mathbf{A_c}_{ij}=[0\ A_{cij}\ 0]^{\text{T}}$ and $\mathbf{A_m}=[0\ A_{mi}\ 0]^{\text{T}}$. Since all elemental sources are relatively static to each other, the time-derivative of A_{cij} is irrelevant to the conductor motion. In contrast, A_{mi} is related to the vibration and its time-derivative is given by (5):

$$\frac{\partial A_{mi}}{\partial t}=\frac{\partial A_m\left(r_i,z_i\right)}{\partial z_i}\frac{dz_i}{dt}=-B_r\left(r_i,z_i\right)w(t) \tag{5}$$

where $r_i=\bar{r}_i$ and $z_i=\bar{z}_i+z(t)$ about an equilibrium position ($\bar{r}_i$, $\bar{z}_i$). Since the conductor vibrates relative to a fixed PM, B_r must be calculated for a specified $z(t)$. For an axial-magnetized cylindrical PM, its MFD field in space can be calculated in an efficient way based on the approach proposed in [18], which is originally derived for the magnetic field of EC. Using similar derivations, the MFD generated by the PM can be obtained as

$$\frac{B_r\left(r_i,z_i\right)}{\mu_0M_0}=-\frac{a_o}{r_b}\sum_{k=1}^{\infty}\frac{\beta_1\left(\psi_k a_o\right)\beta_1\left(\psi_k r_i\right)}{\psi_k r_b\left[\beta_0^2\left(\psi_k r_b\right)\right]}\left(1-e^{-2\psi_k a}\right)e^{\psi_k(a+z_i)} \tag{6}$$

where $\beta_n(x)$ is the n^{th} order Bessel function of the 1st kind; r_b ($>5r_p$) is the truncating radius [18]; $\Psi=x_k/r_b$ and x_k is the k^{th} positive root of the equation $\beta_1(x)=0$. In practical computation, (6) can achieve high accuracy when taking only the first 500 terms.

In matrix forms, with $\mathbf{J}=[J_1\cdots\ J_i\cdots\ J_n]^{\text{T}}$, Eq. (4a) can be written in a state-space representation

$$\dot{\mathbf{J}}(t)=\boldsymbol{\alpha}\mathbf{J}(t)+\boldsymbol{\beta}\mathbf{u}(t) \tag{7}$$

where $\boldsymbol{\alpha} = -(\sigma\mathbf{T})^{-1}$, $\boldsymbol{\beta} = \mathbf{T}^{-1}$, $\mathbf{u}(t) = \mathbf{b}w(t)$ and $\mathbf{T}_{ij} = V_j f(r_{ij})$, $\mathbf{b}(\in \mathbb{R}^{n\times 1}) = [\cdots B_{ri}(r_i, z_i)\cdots]^{\mathrm{T}}$. It should be noted that **b** is a function of the conductor position which is time-varying.

Once **J** is solved, the effects of the ECD, including the Lorentz force **F** on the conductor (which is in the z-direction due to symmetry) and the EC-generated MFD $\mathbf{B_c}$ at the measurement point $\mathbf{r}_s$, can be easily derived from (2) and (3), and given by (8), (9), respectively.

$$F_z = -\mathbf{b}^{\mathrm{T}}\mathbf{V}\mathbf{J} \tag{8}$$

$$\mathbf{B_c}(\mathbf{r}_s) = \begin{bmatrix} B_{sr} & B_{sz} \end{bmatrix}^{\mathrm{T}} = \mathbf{C}\mathbf{J} \tag{9}$$

where $\mathbf{V} = diag\left(\begin{bmatrix} V_1 \cdots & V_i \cdots & V_n \end{bmatrix}\right)$

$$\mathbf{C} = \begin{bmatrix} V_1\mathbf{g}(\mathbf{r}_{s1})\cdots & V_i\mathbf{g}(\mathbf{r}_{si})\cdots & V_n\mathbf{g}(\mathbf{r}_{sn}) \end{bmatrix}$$

$$\mathbf{g}(\mathbf{r}_{si}) = \frac{\mu_0}{4\pi}\int_0^{2\pi} \frac{\begin{bmatrix} (z_s - z_i)\cos\theta & r_i - r_s\cos\theta \end{bmatrix}^{\mathrm{T}} d\theta}{\left[(r_s - r_i\cos\theta)^2 + (r_i\sin\theta)^2 + (z_s - z_i)^2 \right]^{3/2}}$$

B. ECD solutions

Given $z(t)$, Eq. (7) can be discretized with a zero-order hold (with a sampling period of ΔT) resulting in (10) which can be solved iteratively to obtain the discrete-time solutions of the ECD **J** in the vibrating conductor:

$$\mathbf{J}(k+1) = e^{\boldsymbol{\alpha}\Delta T}\mathbf{J}(k) + \int_0^{\Delta T} e^{\boldsymbol{\alpha}\lambda} d\lambda \mathbf{u}(k) \tag{10}$$

The effects of the two commonly made assumptions in literatures [4, 7, 16] on the solutions to the motion-induced ECD field are discussed:

Assumption 1 (A1) neglects the effects of mutual induction (MI). The ECD is only contributed by the PM magnetic field and the conductor motion:

$$\mathbf{J}(t) = \sigma\mathbf{b}w(t) \tag{11}$$

Assumption 2 (A2): The vibration displacement is small such that $B_r(r_i, z_i) \approx B_r(\bar{r}_i, \bar{z}_i)$, and hence, **b** is a constant vector.

- The motion-induced ECD in the vibrating conductor is equivalent to that induced by a harmonic excitation.
- The closed-form frequency response (steady-state solutions) to the ECD can be derived in (11) using a phaser method which takes on the form of $\dot{\mathbf{J}} = j\omega\mathbf{J}$, where $j = \sqrt{-1}$, **I** is $n\times n$ identity matrix.

$$\mathbf{J} = \omega\sigma Z_o \left(j\omega\sigma\mathbf{I} + \mathbf{T}^{-1} \right)^{-1} \mathbf{T}^{-1}\mathbf{b} \tag{12}$$

- Eq. (12) implies that the conductivity σ and vibration frequency ω, both of which influence the induced ECD, can be characterized by a single parameter: skin-depth δ $(= \sqrt{2/(\mu_0\omega\sigma)})$.

III. Results and Discussions

The proposed method for modeling the motion-induced EC in a vibrating conductor has been evaluated. Solutions that were computed for the 2D axis-symmetric setup (Fig. 1), along with the parametric values in Table I, are organized as follows:

1) For validation, the DCS-based solutions are compared with FEA in Fig. 2(a, b) where the commercial (COMSOL Multiphysics) software was used as a basis for comparisons. In COMSOL, the *moving mesh* method was used to simulate a moving PM that vibrates above the conductor, which is equivalent to having a conductor vibrate under a static PM.

   Table I (left column) is a partial view of the mesh, where the vertical space directly above/below the PM was re-meshed at each time step to accommodate the relative motion of the PM. A fixed air space is included around the deformable space and the conductor. A forced harmonic vibration is prescribed to the PM; thus, the vibration displacement and velocity are not influenced by the damping force. The calculation time-step is set to 1% of the vibration period.
2) The effects of two commonly used assumptions on the computational accuracy are numerically examined:
   a. The effects of Assumption 1 on the ECD, EC-generated MFD and damping force are presented in Fig. 2 where the responses with and without accounting for the mutual induction are compared.
   b. The effects of Assumption 2 (small vibration) on the accuracy of the damping force computation are illustrated in Fig. 3 where the solutions of the DCS model and that of the simplified model (12) are compared in time domain (Fig. 3a) and in frequency domain (Fig. 3b).
3) To facilitate design optimization, the parametric effects of the PM aspect ratio and conductor skin-depth (accounting for the electrical conductivity and vibration frequency) on the damping force are presented in Figs. 4, 5 and 6.

Table I. Parametric values used in numerical investigation

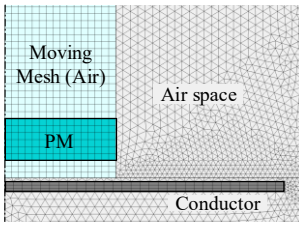

PM	(a_o, a) = (16, 3) mm $\mu_0 M_0$:1.465T
Conductor	$(r_p, h; d)$ = (40,1.5, 6) mm σ = 33.5MS/m f = 50, 200Hz, Z_o = 1mm
Sensor	(r_s, z_s) = (6, -12) mm
Mesh size	1×0.75mm (DCS) Max. 0.9mm (FEA)
Time step	dt = 1/ (100 f)

A. Numerical validation

Fig. 2(a) compares the DCS-modeled ECD (1st row), EC-generated MFD (2nd row) and damping force (3rd row) with the FEA simulated in COMSOL and with the simplified model that ignores mutual induction (MI) for two vibration frequencies (f = 50 and 200Hz); all in the time domain. In the 1st row, the average ECD values at r = 20mm are plotted. The 2nd row plots the simulated "measured-MFD" in the r-direction at (6, −12) mm, while the 3rd row plots the damping force exerted on the conductor. Fig. 2(b) shows the circumferential component of the average ECD along the conductor radius when $z(t)$ reaches its positive peak position corresponding to t = 30ms (f = 50) and t = 7.5ms (200Hz). Fig. 2(c) illustrates the MI effects on the amplitude/phase of the damping force over a range of vibrating frequencies, where the DCS models with and without accounting for MI are compared with a constant vibration amplitude of 1mm.

Fig. 3 compares the damping force calculated from the DCS model and a simplified model with small vibration assumption (12). Vibrations of two amplitudes (Z_o = 0.5mm and 2mm) for a given frequency (f = 200Hz) are simulated to compare the damping force in both time domain (Fig. 3a) and frequency

domain (Fig. 3b). The first four orders of the harmonic components are further shown in Fig. 3(c) as vibration amplitudes varies from 0 to 2mm. The following observations can be obtained from Figs. 2 and 3.

– As compared in Fig. 2(a, b), the DCS-modeled transient responses of the ECD, EC-generated MFD and damping force show excellent agreements with FEA for both 50Hz and 200Hz vibrations, demonstrating the accuracy of the model in the order of 1% difference relative to FEA simulated in COMSOL. At 50Hz, the simplified model without MI almost agree with the FEA, with a difference in peak damping force of 2.1%. However, the model without MI at 200Hz show a significant discrepancy from FEA and DCS (considering MI) for both the magnitude and phase, with a difference of 13.8%.

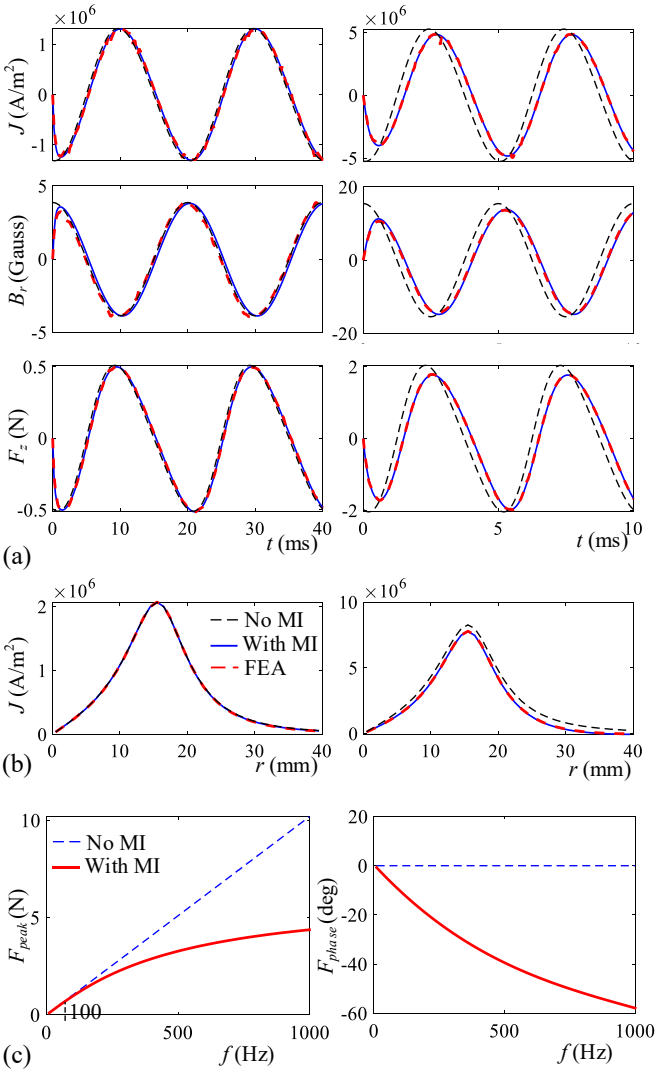

Fig. 2 Results. (a) DCS and FEA at 50Hz (left) and at 200Hz (right): ECD (1st row), EC-generated MFD (2nd row) and damping force (3rd row). (b) ECD along the radius at 50Hz (left) and at 200Hz (right). (c) Damping force with/without MI: peak (left) and phase (right).

– Fig. 2(c) illustrates the frequency effects on the peak magnitude (left column) and phase (right column) of the computed damping force. At a relatively low vibration frequency (f <100Hz), the peak damping forces calculated from the models (with or without considering MI) are almost the same. However, the MI effects on the peak damping force cannot be neglected as frequency increases. As shown in the phase plot of the damping force, the phase lag is not observed in the simplified model.

– As revealed in Fig. 3(b), the 0th order component (though very weak) is not zero indicating that the damping force is asymmetrical. As a result, high-order harmonic components appear in the damping force because the PM-generated MFD varies and is asymmetric about the equilibrium position as the conductor vibrates to different position.

– As compared in Fig. 3(a, b) between small vibration (Z_o=0.5mm, left) and large vibration (Z_o=2mm, right), the small-amplitude assumption that yields sinusoidal responses in all cases fails to capture the higher-order harmonics.

– As shown in Fig. 3(c) where the (0th, 1st, 2nd and 3rd)-order harmonic components are plotted against the vibration amplitude, the 1st order magnitude is linear with Z_o and closely similar to the small-vibration model characterized solely by the 1st order. The 2nd order magnitude is approximately quadratic relative to Z_o and is significantly larger than the 0th and 3rd order magnitudes. In contrast, the phases of all components are constant when Z_o increases.

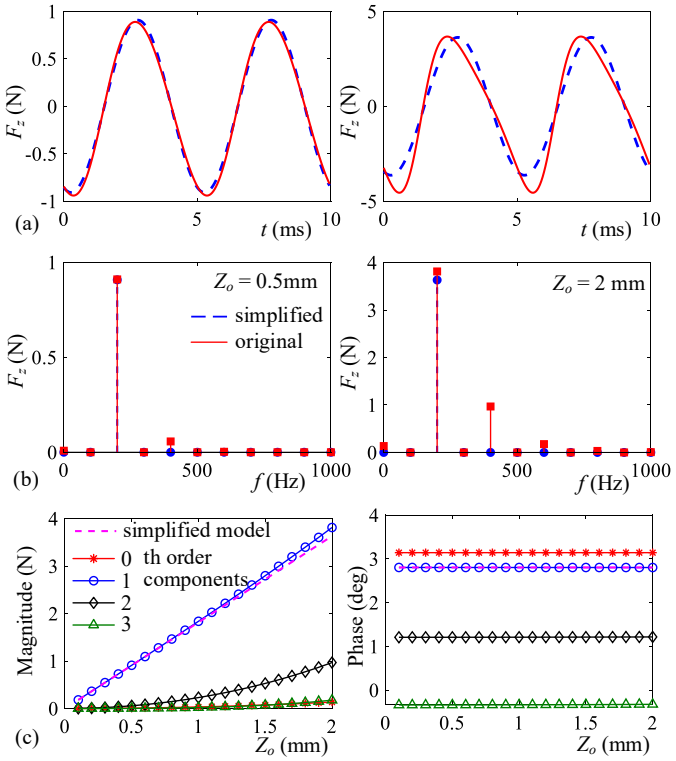

Fig. 3 Effects of small vibration assumption on damping force (a) Time-domain. (b) Frequency domain. (c) Magnitude and phase of first four order components over a range of vibration amplitudes.

B. Parametric effects on damping force

To provide guidelines to optimize EC damping forces, a numerical study was conducted to investigate the effects of the PM aspect ratio (height-to-diameter ratio) and the skin depth on the damping force generated by the motion-induced EC.

PM aspect ratio

Fig. 4 shows the effects of PM aspect ratio ($\rho = a/a_o$) on the damping force for a given PM volume (Table I). The

magnitudes of the damping force at its 1st order frequency are plotted for two vibration frequency values at the given vibration amplitude, Z_o = 1mm. As shown in Fig. 4, for both frequencies, the magnitudes of the damping force increase with the decrease of aspect ratio and reach the maxima when ρ = 0.4 (corresponding to a_o = 12.5mm and a = 5mm). As the PM becomes flatter, the damping force decreases. In general, a flat PM can generate larger damping force than a tall and slim PM.

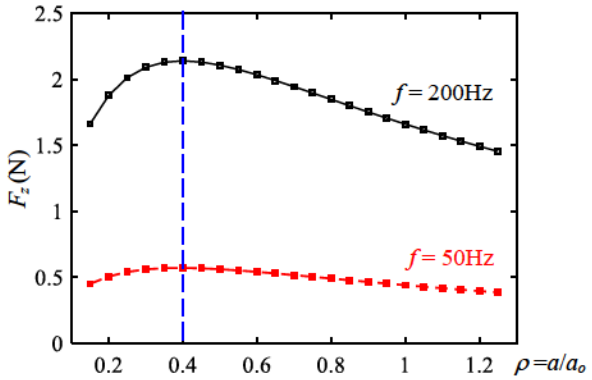

Fig. 4 Effects of PM aspect ratio on damping force.

Skin-depth (conductivity and frequency)

The conductivity can greatly affect the induced ECD and hence the damping force. Fig. 5 compares the damping force exerted on different metals with different conductivities (ranging from 2.98MS/m to 59.6MS/m). Among the 4 metals selected for the study, the widely used copper (Cu) and titanium (Ti) have the highest and lowest conductivities, respectively. As in (4a), the material with a higher conductivity that results in a higher induced ECD experiences a larger damping force under the same magnetic field. The coupled effects of different conductivity and MI not only result in magnitude differences, but also noticeable phase difference among the damping forces of four different conductors. With that being said, neglecting MI will not only introduce errors in the computed magnitude, but also in the phase of the eddy current (and damping force), especially when σ is a large value.

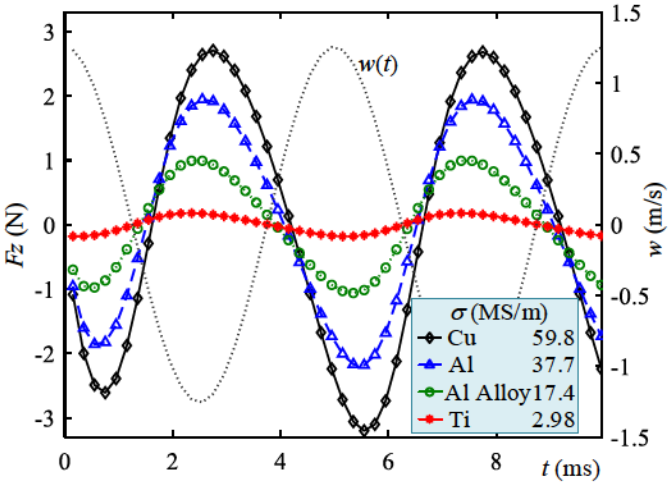

Fig. 5 Damping force on a conductor of different electric conductivity in time-domain.

In Fig. 6, an in-depth study about the effects of conductivity and frequency on damping force is conducted, which plots the 1st order components of the damping force for three of the four abovementioned materials (Cu, Al alloy and Ti) as the vibration frequency varies from 100Hz to 1000Hz. The magnitude and phase of the damping force with respect to the normalized skin depth Δ ($= \delta/a$), which accounts for frequency and conductivity simultaneously, are plotted in Fig. 6(a) and 6(b), respectively. The same procedure is repeated for four different conductor thicknesses H ($=h/a$).

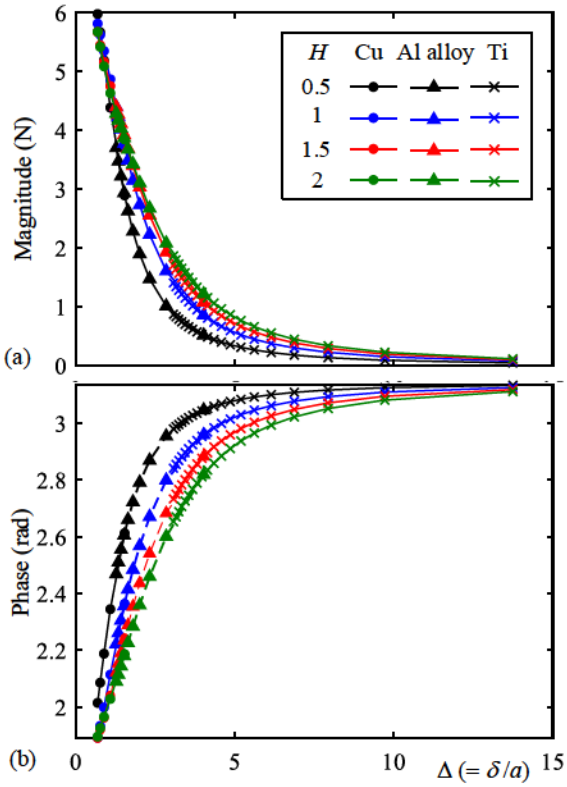

Fig. 6 Magnitude and phase of 1st order harmonic damping force for different skin depths. (a) Magnitude. (b) Phase.

The following observations can be found from Fig. 6:

- For each fixed H, the magnitude and phase curves of the three materials almost overlap at the same δ values. In other words, conductors of different materials experience the same damping force so long as their skin depth are the same, demonstrating that the skin depth δ alone can characterize the effects of f and σ.
- The upper left region in Fig 6(a) shows that the lines plotted for different H merge when Δ is small, which corresponds to a high f or a high σ, indicating that the conductor thickness does not have a significant impact on the damping force when Δ is small. On the other hands, when Δ is relatively larger, the separating lines indicate that the thickness of the conductor has more effect on the eddy current and the damping force.
- Fig. 6(b) shows the phase change with Δ. Much alike the magnitude and Δ relation, with small Δ, the phase lag is not heavily dependent on the conductor thickness. But when Δ is large, the conductor thickness has more impact on the phase difference, with thicker conductors having larger phase lag. For large Δ (or low vibration frequency), the phase shift with respect to the vibrating frequency is close to π (180°), that is, the induced damping force always opposes the conductor

Manuscript 324 submitted to IEEE/ASME International Conference on Advanced Intelligent Mechatronics. Received March 7, 2019.

vibration. However, for small Δ, the anti-phase relation no longer holds, which must be taken into consideration in the design and control of EC dampers.

IV. Conclusion

A distributed parameter state-space model based on DCS method has been developed for describing the motion-induced ECD, the EC-generated MFD, and the damping force on a vibrating conductor under a static magnetic field. The model shows accurate performance when compared against FEA simulation. The difference between the two methods is between 0.04% and 1.15% for different vibration frequencies. The model was used to study the accuracy of simplified models that either assume no MI or regard the MFD as constant within the range of small vibration. The results demonstrate that at low frequencies (<100Hz), the results without considering MI is very close to that with MI, but at high frequencies, both magnitude and phase show discrepancies, with a peak damping force difference of 13.8% for vibration at 200Hz, and an increased phase difference. The study also shows that assuming constant MFD could yield accurate results when displacement is small, but with larger displacement, higher order harmonic components can no longer be ignored.

Parametric study about the PM aspect ratio was conducted and the optimal parameters can be determined to achieve maximum damping force. A study on skin depth shows that the damping force can be formulated such that it is solely dependent on the skin depth, and that it becomes independent of the conducting material so long as the skin depth is fixed. Further study on the skin depth shows that when the skin depth is small, i.e. high vibration frequency, the damping force and its phase difference is not heavily dependent on the conductor thickness. The large phase difference at small Δ indicates that the damping force cannot generate a purely anti-motion effect. However, for large Δ, the phase shift is almost nonexistent.

Although the system discussed in this paper is axisymmetric and forced vibration, the same concept can be extended to non-symmetric and more general vibration cases. Besides that, the state-space model makes it possible for applying control theory in active damping studies.

Reference

[1] J. R. Reitz, "Forces on moving magnets due to eddy currents," *Journal of Applied Physics,* vol. 41, no. 5, pp. 2067-2071, 1970.

[2] K. Karakoc, A. Suleman, and E. J. Park, "Optimized braking torque generation capacity of an eddy current brake with the application of time-varying magnetic fields," *IEEE Transactions on Vehicular Technology,* vol. 63, no. 4, pp. 1530-1538, 2014.

[3] J.-S. Bae, J.-H. Hwang, J.-H. Roh, J.-H. Kim, M.-S. Yi, and J. H. Lim, "Vibration suppression of a cantilever beam using magnetically tuned-mass-damper," *Journal of Sound and Vibration,* vol. 331, no. 26, pp. 5669-5684, 2012.

[4] J. Laborenz, C. Siewert, L. Panning, J. Wallaschek, C. Gerber, and P.-A. Masserey, "Eddy current damping: a concept study for steam turbine blading," *Journal of Engineering for Gas Turbines and Power,* vol. 132, no. 5, pp. 052505-052505-7, 2010.

[5] B. Ebrahimi, M. B. Khamesee, and M. F. Golnaraghi, "Design and modeling of a magnetic shock absorber based on eddy current damping effect," *Journal of Sound and Vibration,* vol. 315, no. 4, pp. 875-889, 2008.

[6] B. Ebrahimi, M. B. Khamesee, and F. Golnaraghi, "Permanent magnet configuration in design of an eddy current damper," *Microsystem Technologies,* vol. 16, no. 1, pp. 19, 2008.

[7] Y. Yang, D. Xu, and Q. Liu, "Vibration suppression of thin-walled workpiece machining based on electromagnetic induction," *Materials and Manufacturing Processes,* vol. 30, no. 7, pp. 829-835, 2015.

[8] Y. Yang, D. Xu, and Q. Liu, "Milling vibration attenuation by eddy current damping," *The International Journal of Advanced Manufacturing Technology,* vol. 81, no. 1, pp. 445-454, 2015.

[9] H. A. Sodano, and D. J. Inman, "Non-contact vibration control system employing an active eddy current damper," *Journal of sound and vibration,* vol. 305, no. 4-5, pp. 596-613, 2007.

[10] H. Zhu, C. K. Pang, and T. J. Teo, "Analysis and control of a 6 DOF maglev positioning system with characteristics of end-effects and eddy current damping," *Mechatronics,* vol. 47, pp. 183-194, 2017.

[11] J. Wu, Y. Sun, B. Feng, and Y. Kang, "The effect of motion-induced eddy current on circumferential magnetization in MFL testing for a steel pipe," *IEEE Transactions on Magnetics,* vol. 53, no. 7, pp. 1-6, 2017.

[12] N. Esposito, A. Musolino, and M. Raugi, "Modelling of three-dimensional nonlinear eddy current problems with conductors in motion by an integral formulation," *IEEE transactions on Magnetics,* vol. 32, no. 3, pp. 764-767, 1996.

[13] P. Ying, R. Jiangjun, Z. Yu, and G. Yan, "A composite grid method for moving conductor eddy-current problem," *IEEE Transactions on Magnetics,* vol. 43, no. 7, pp. 3259-3265, 2007.

[14] K. Muramatsu, N. Takahashi, T. Hashio, C. Yamada, M. Ogawa, S. Kobayashi, and T. Kuwahara, "3-D eddy current analysis in moving conductor of permanent magnet type of retarder using moving coordinate system," *IEEE Transactions on Energy Conversion,* vol. 14, no. 4, pp. 1312-1317, 1999.

[15] K. Pluk, T. Van Beek, J. Jansen, and E. A. Lomonova, "Modeling and measurements on a finite rectangular conducting plate in an eddy current damper," *IEEE Transactions on Industrial Electronics,* vol. 61, no. 8, pp. 4061-4072, 2014.

[16] H. A. Sodano, J.-S. Bae, D. J. Inman, and W. K. Belvin, "Concept and model of eddy current damper for vibration suppression of a beam," *Journal of Sound and Vibration,* vol. 288, no. 4-5, pp. 1177-1196, 2005.

[17] C. Lin, K. Lee, and B. Hao, "Distributed current source method for modeling magnetic and eddy-current fields induced in nonferrous metallic objects," *IEEE/ASME Transactions on Mechatronics,* vol. 23, no. 3, pp. 1038-1049, 2018.

[18] Y. Li, T. Theodoulidis, and G. Y. Tian, "Magnetic field-based eddy-current modeling for multilayered specimens," *IEEE Transactions on Magnetics*, vol. 43, no. 11, pp. 4010-4015, 2007.